Numerical Heat Transfer, Part A: Applications: An International Journal of Computation and Methodology
Publication details, including instructions for authors and subscription information:
http://www.tandfonline.com/loi/unht20

HEAT AND FLUID FLOW ACROSS A SQUARE CYLINDER IN THE TWO-DIMENSIONAL LAMINAR FLOW REGIME

Atul Sharma [a] & V. Eswaran [a]
[a] Department of Mechanical Engineering, Kanpur, India
Published online: 17 Aug 2010.

To cite this article: Atul Sharma & V. Eswaran (2004): HEAT AND FLUID FLOW ACROSS A SQUARE CYLINDER IN THE TWO-DIMENSIONAL LAMINAR FLOW REGIME, Numerical Heat Transfer, Part A: Applications: An International Journal of Computation and Methodology, 45:3, 247-269

To link to this article: http://dx.doi.org/10.1080/10407780490278562

Numerical Heat Transfer, Part A, 45: 247–269, 2004

ISSN: 1040-7782 print/1521-0634 online
DOI: 10.1080/10407780490278562

Taylor & Francis
Taylor & Francis Group

HEAT AND FLUID FLOW ACROSS A SQUARE CYLINDER IN THE TWO-DIMENSIONAL LAMINAR FLOW REGIME

Atul Sharma and V. Eswaran
Department of Mechanical Engineering, Indian Institute of Technology, Kanpur, India

The flow structure and heat transfer characteristics of an isolated square cylinder in cross flow are investigated numerically for both steady and unsteady periodic laminar flow in the two-dimensional regime, for Reynolds numbers of 1 to 160 and a Prandtl number of 0.7. The effect of vortex shedding on the isotherm patterns and heat transfer from the cylinder is discussed. Heat transfer correlations between Nusselt number and Reynolds number are presented for uniform heat flux and constant cylinder temperature boundary conditions.

1. INTRODUCTION

A bluff body is one in which the flow, under normal circumstances, separates from a large section of the body surface, thus creating a significant wake region downstream. Over the past hundred years or so, the flow around bluff bodies has posed a challenging fluid mechanics problem involving the interaction of three shear layers, namely, a boundary layer, a separating free shear layer, and a wake, each with different or coupled processes of developing instabilities as the Reynolds number is increased. Such flows represent an important class of engineering applications. The nature of the flow determines device performance affecting force, vibration, or heat transfer rates for many engineering applications. Bluff-body-induced flow unsteadiness and mixing may also be used to enhance heat and mass transfer between the body and its surroundings.

These flows can be classified according to the number, arrangement, and cross-sectional shapes of the bluff bodies, the character of the approaching flow, and whether it is free-stream or of a confined type. Most research in the past has been focused on circular cylinders. Excellent reviews on this configuration have been written by Zdravkovich [1] and Williamson [2]. The flow past a square cylinder resembles flow past a circular cylinder as far as instabilities are concerned, but the separation mechanism and the consequent dependence of the shedding frequency and the aerodynamic forces on the Reynolds number differ significantly. Unlike the circular cylinder, the separation points of the square cylinder are fixed at its leading or trailing edges. Furthermore, the width of the wake immediately behind the

Received 18 March 2003; accepted 23 June 2003.
Address correspondence to Prof. Vinayak Eswaran, Department of Mechanical Engineering, Indian Institute of Technology, Kanpur 208016, India. E-mail: eswar@iitk.ac.in

NOMENCLATURE

B	width of the square cylinder	T_∞	free-stream temperature
c_p	specific heat of the fluid	u	streamwise velocity
CV	control volume	u_∞	free-stream velocity
C_D	total drag coefficient $(= C_{Dp} + C_{Dv})$	U	nondimensional streamwise velocity $(= u/u_\infty)$
C_{Dp}	pressure drag coefficient $(= F_{Dp}/\frac{1}{2}\rho u_\infty^2 B)$	U_c	average nondimensional streamwise velocity
C_{Dv}	viscous drag coefficient $\left(= F_{Dv}/\frac{1}{2}\rho u_\infty^2 B\right)$	v	cross-stream velocity
C_L	lift coefficient $\left(= F_L/\frac{1}{2}\rho u_\infty^2 B\right)$	V	nondimensional cross-stream velocity $(= v/u_\infty)$
f	frequency of vortex shedding	x	streamwise dimension of coordinates
F_{Dp}	pressure drag force on the cylinder	X	nondimensional streamwise dimension of coordinates $(= x/B)$
F_{Dv}	viscous drag force on the cylinder	y	cross-stream dimension of coordinates
F_L	lift force on the cylinder	Y	nondimensional cross stream dimension of coordinates $(= y/B)$
H	height of the computational domain	β	blockage ratio $(= B/H)$
k	thermal conductivity of the fluid	δ	size of the CV clustured around the cylinder
L	nondimensional length of the computational domain	Δ	size of the CV far away from the cylinder
L_D	nondimensional distance between the rear surface of the cylinder and the exit plane	θ	nondimensional temperature
L_r	recirculation length	μ	dynamic viscosity of the fluid
L_U	nondimensional distance between the inlet plane and the front surface of the cylinder	ρ	density of the fluid
M	number of grid points in X direction	τ	nondimensional time $[= t/(B/u_\infty)]$
n	cylinder surface normal direction	ϕ	dependent variable in the convective boundary condition
N	number of grid points in Y direction		
Nu	average Nusselt number		
p	pressure	**Subscripts**	
P	nondimensional pressure $(= p/\rho u_\infty^2)$	b	bottom face of the cylinder
Pr	Prandtl number $(= \mu c_p/k)$	c	cylinder average
q	heat flux	f	front face of the cylinder
Re	Reynolds number $(= \rho u_\infty B/\mu)$	r	rear face of the cylinder
St	Strouhal number $(= fB/u_\infty)$	rms	root mean square
t	time	t	top face of the cylinder
T	temperature	W	surface of the cylinder

cylinder is at least one diameter, whereas it is less than half a diameter in the case of a circular cylinder. Consequently, the Kármán vortex formation region is significantly longer and broader for the square cylinder than for the circular cylinder. The square cylinder is a more bluff body than circular cylinder. From an engineering point of view, flow around structures that typically have rectangular or near-rectangular cross sections—i.e., buildings, electronic equipments, etc.—are more akin to flow around square cylinders than circular ones. Thus, the flow around the square cylinder is an important fundamental problem of engineering interest.

The isothermal, nonconfined flow past a cylinder of square or rectangular cross section has been investigated both numerically and experimentally [3–17]. However, most of the experimental work has been performed for the turbulent regime (see examples in [1]). Zaki et al. [9] have done numerical investigation at low Reynolds number and experimental investigation at high Reynolds number for flow

past a square cylinder. Sohankar et al. [10] have done numerical simulations of two-dimensional flow past a square cylinder at $Re = 45$–250. Quantities such as drag and lift coefficients, various surface pressure coefficients, and the mean vortex formation length behind the cylinder have been calculated for different Reynolds numbers. Okajima [12] studied the effect of blockage on a stationary and oscillating cylinder. Sohankar et al. [13] also studied the effect of blockage, onset of vortex shedding, and influence of outlet boundary conditions for the flow past the square cylinder at angle incidence of 0–45° and $Re = 45$–200. Caughey [14] applied the implicit multigrid method for laminar flow past stationary and moving cylinders of square cross section. Furthermore, Sohankar et al. [15] carried out 2-D and 3-D unsteady flow simulations for the same configuration at moderate Reynolds number ($Re = 150$–500) and a blockage ratio of 5.6%. They found a stable 2-D laminar (vortex) shedding flow at $Re = 150$, and the corresponding 3-D flow at $Re = 200$, without determining the exact Reynolds number at which the transition from 2-D to 3-D occurs. Robichaux et al. [16] studied the onset of three-dimensionality in the periodic wake of a square cylinder using Floquet stability analysis to extract the different modes of 3-D instabilities. They performed the 2-D simulations using a spectral multidomain technique to establish the time-periodic base state. They found that the 3-D disturbance first becomes unstable at a Reynolds number of about 161. Therefore, the Reynolds number of 160 was chosen as the upper limit for the present computations, which are confined to the two-dimensional regime. Recently, Saha et al. [17] found the transition to three-dimensionality to occur at a Reynolds number between 150 and 175.

An account of many of the experimental results and correlations for forced-convection heat transfer from a circular cylinder has been given by Morgan [18]. There are comparatively fewer numerical studies on this topic than for isothermal flow past a circular cylinder. Dennis et al. [19] obtained the numerical solution for the steady laminar forced convection from a circular cylinder. Karniadakis [20] used the spectral element method to obtain forced-convection heat transfer from an isolated circular cylinder in cross flow, for both steady and (unsteady) periodic flow, for $Re \leq 200$. He obtained transient results at $Re = 50$, 100, and 200 for the constant cylinder temperature and constant heat flux cases. Yang et al. [21] obtained the numerical solution for the transient laminar forced convection from a circular cylinder at $Re = 100$, 200, and 500. Lange et al. [22] have done a numerical investigation of the 2-D flow around a heated circular cylinder considering the temperature dependence on the fluid properties.

Although some information is available on the forced-convection heat transfer from an isolated circular cylinder in cross flow, virtually no analogous results are available for the square cylinder, although Igarashi [23] has experimentally investigated the problem for much higher Reynolds numbers. Kelkar et al. [24] numerically predicted the Nusselt number for the square cylinder maintained at constant temperature for $Re = 100$, but their main focus was on the onset of unsteadiness.

The objective of the present work is to study free-stream flow over a square cylinder and explore the link between heat transfer and the various 2-D laminar flow regimes for the two classical boundary conditions: uniform temperature and uniform heat flux. Although the flow regimes have been studied previously, the

steady and unsteady heat transfer from a square cylinder, which is the focus of the present work, is largely unexplored. An objective of this work is to generate a numerical database for the flow and heat transfer parameters with respect to Reynolds number, and to develop heat transfer correlations between Nusselt number and Reynolds number in the regime for the boundary conditions considered.

2. PHYSICAL DESCRIPTION OF THE PROBLEM

The flow configuration is shown in Figure 1. A fixed two-dimensional square cylinder with side B, which is also the nondimensionalizing length scale, is exposed to a constant free-stream velocity and temperature represented by u_∞ and T_∞, respectively. In order to make the problem computationally feasible, artificial confining boundaries are placed around the flow, where free slip boundary conditions are used. The ratio of the width of the cylinder to the vertical distance between the upper and lower walls, H, defines the blockage ratio ($\beta \equiv B/H$) of the confined flow. Sohankar et al. [13] have done a detailed investigation of the effect of blockage in this configuration. They have shown that the boundaries are sufficiently far away if $H = 20B$ (i.e., $\beta = 5\%$), and their presence has little effect on the characteristics of the flow near the cylinder. Thus, $H = 20B$ has been used in the present work. The nondimensional distance between the inlet plane and the front surface of the cylinder, L_U, is 8.5, and the nondimensional distance between the rear surface of the cylinder and the exit plane, L_D, is 16.5, with the total nondimensional length of the computational domain $L = 26$.

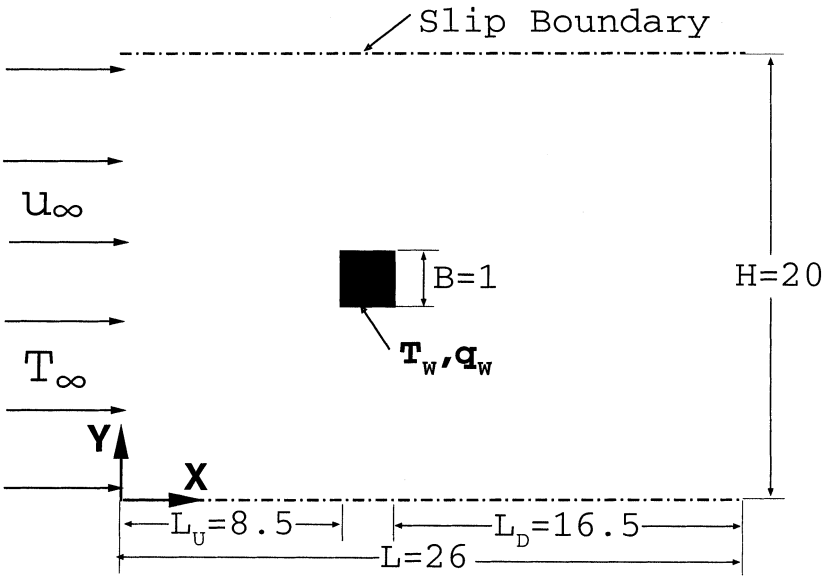

Figure 1. Computational domain for the flow around a square cylinder and the associated parameters.

3. MATHEMATICAL FORMULATION

The governing equations and the boundary conditions for the flow and temperature field are discussed below.

3.1. Flow Field

The unsteady, conservative, dimensionless form of the Navier–Stokes equations in two dimensions for the incompressible flow of a constant viscosity fluid is given as follows.

x Momentum:

$$\frac{\partial U}{\partial \tau}+\frac{\partial (UU)}{\partial X}+\frac{\partial (VU)}{\partial Y}=-\frac{\partial P}{\partial X}+\frac{1}{\mathrm{Re}}\left(\frac{\partial^2 U}{\partial X^2}+\frac{\partial^2 U}{\partial Y^2}\right) \tag{1}$$

y Momentum:

$$\frac{\partial V}{\partial \tau}+\frac{\partial (UV)}{\partial X}+\frac{\partial (VV)}{\partial Y}=-\frac{\partial P}{\partial Y}+\frac{1}{\mathrm{Re}}\left(\frac{\partial^2 V}{\partial X^2}+\frac{\partial^2 V}{\partial Y^2}\right) \tag{2}$$

Continuity:

$$\frac{\partial U}{\partial X}+\frac{\partial V}{\partial Y}=0 \tag{3}$$

with

$$U=\frac{u}{u_\infty} \qquad V=\frac{v}{u_\infty} \qquad \tau=\frac{tu_\infty}{B} \qquad X=\frac{x}{B} \qquad Y=\frac{y}{B} \qquad P=\frac{p}{\rho {u^2}_\infty} \tag{4}$$

Here u_∞ is the uniform velocity of the fluid far away from the cylinder.

The Reynolds number is the only governing flow parameter for this problem and is defined as $\mathrm{Re}=\rho u_\infty B/\mu$.

The boundary condition are as follows:

Top and bottom artificial boundaries: $\left(\frac{\partial U}{\partial Y}\right)=0, V=0$
Solid surface of the cylinder: $U=0, V=0$
Left boundary (inlet): $U=1, V=0$
Right boundary (outlet): The convective boundary condition (CBC), given by

$$\frac{\partial \phi}{\partial \tau}+U_c\frac{\partial \phi}{\partial X}=0$$

has been used, with the average nondimensional streamwise velocity $U_c=1$ and ϕ the dependent variable U or V. Sohankar et al. [13] have compared the CBC with the Neumann boundary condition (NBC) at the outlet for the present configuration

and show that the CBC is better, as it decreases the number of iterations per time step and the number of time steps to reach periodic flow, and allows lower L_D to be used.

3.2. Temperature Field

The temperature field is computed for the conditions of uniform heat flux and constant cylinder temperature. The cylinder exchanges heat with the cold fluid flowing around it, which is at a uniform temperature (T_∞) far away from the cylinder.

The unsteady dimensionless form of the energy equation (assuming negligible viscous dissipation) is given as

$$\frac{\partial \theta}{\partial \tau} + \frac{\partial (U\theta)}{\partial X} + \frac{\partial (V\theta)}{\partial Y} = \frac{1}{\mathrm{Re}\,\mathrm{Pr}} \left(\frac{\partial^2 \theta}{\partial X^2} + \frac{\partial^2 \theta}{\partial Y^2} \right) \tag{5}$$

where $\theta = T - T_\infty/(T_W - T_\infty)$ for the constant cylinder temperature case and $\theta = (T - T_\infty)/(q_W B/k)$ for the uniform heat flux case. Here T_W is the constant cylinder temperature and q_W is the uniform heat flux dissipating from the cylinder.

The Prandtl number is the only governing heat transfer parameter for this problem and is defined as $\mathrm{Pr} = \mu c_P/k$.

The boundary condition for the temperature field are as follows:

Top and bottom artificial boundaries: $(\partial\theta/\partial Y) = 0$
Solid surface of the cylinder: $\theta = 1$ for constant cylinder temperature case; $(\partial\theta/\partial n) = -1$ for uniform heat flux case, where n represents the direction normal to the surface of the cylinder.
Left boundary (inlet): $\theta = 0$
Right boundary (outlet): $(\partial\theta/\partial\tau) + U_c(\partial\theta/\partial X) = 0$, with $U_c = 1$.

4. NUMERICAL DETAILS

4.1. Grid Structure

A thorough investigation was conducted, using various types of stretching functions, to determine the grid that best captured the unsteady flow features present in the flow calculations. The grid structure which gave the best results is used and is shown in Figure 2. The grid is divided into five separate zones in both directions, and uniform as well as nonuniform grid distributions are employed. The grid distribution was made uniform with a constant cell size, $\Delta = 0.25$, outside a region around the cylinder that extended 4 units upstream, downstream, and sideways. A grid of much smaller size, δ, is clustered around the cylinder over a distance of 1.5 units to adequately capture wake–wall interactions. The hyperbolic tangent function is used for stretching the cell sizes between these limits (δ and Δ). This type of stretching in nonuniform grid distribution has been discussed by Thompson et al. [25]. They reported that the best choices for stretching points when the variation of spacing is large are the hyperbolic tangent and the hyperbolic sine functions, with the former having a better overall distribution.

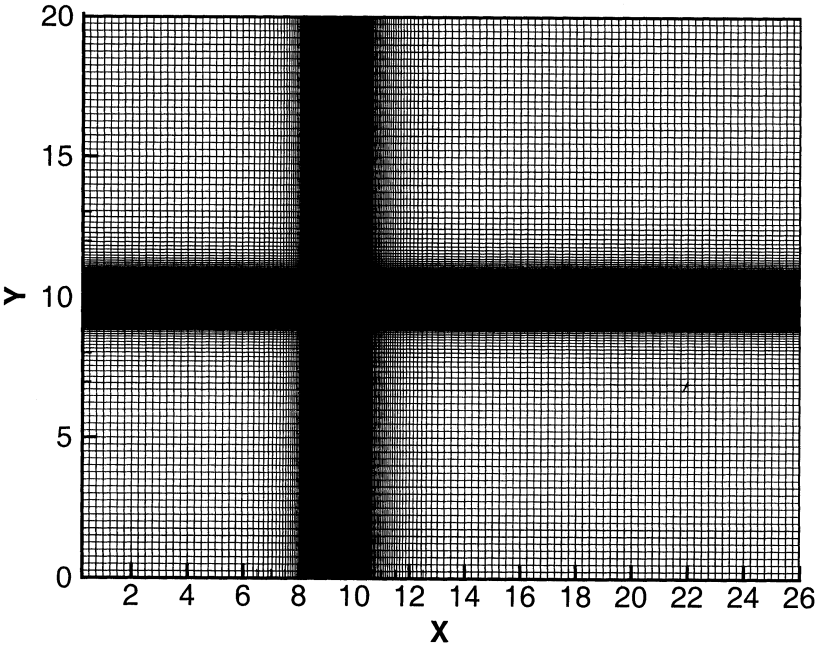

Figure 2. Non-uniform computational grid structure with 323×264 grids.

4.2. Dependence on Grid Size, Time Step, and Initial Condition

Franke et al. [7] and Sohankar et al. [13] have suggested that the distance of the first grid point away from the cylinder has a strong influence on the results. Six grids given in Table 1 are used in the grid-resolution study. Figure 3 shows the results of the grid study done at the highest Reynolds number of 160 used in the present work. It clearly shows that most of the engineering parameters have a monotonic increase or decrease in their values and approach a limiting value as the grid size is increased. An examination of the flow and heat transfer parameters indicates that the grid size $(M \times N)$ of 323×264 is sufficiently fine to obtain results that are essentially grid-independent. It is found that the root-mean-square(rms) value of the coefficient of lift, as compared to the other parameters, has the greatest sensitivity to the number of grid points in the domain and has a maximum difference of 14% and 1.8% on the first two grid sizes when compared to the finest grid size. The percentage change in

Table 1. Overview of all the grids used

S. no.	Number of uniform CVs in the clustered region ($1.5B$ around the cylinder)	Cell size (δ)	Grid size ($M \times N$)
1	36	0.041667	165×132
2	72	0.020834	220×176
3	90	0.016667	245×198
4	120	0.012500	285×232
5	150	0.010000	323×264
6	180	0.008334	363×300

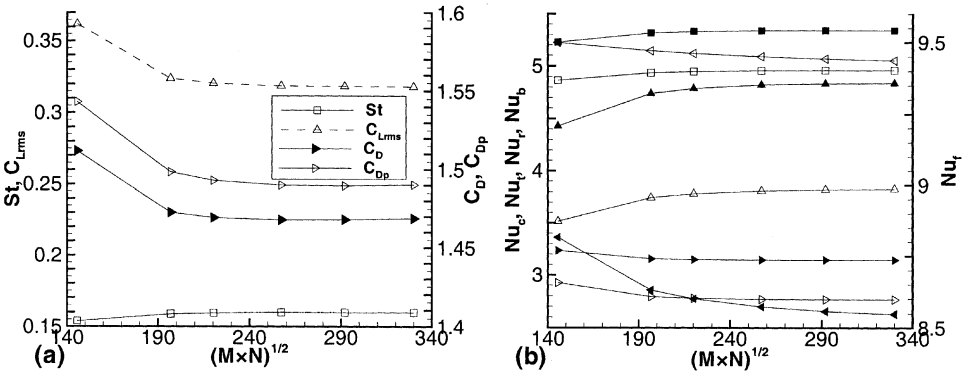

Figure 3. Grid independence results at Re = 160 for the (*a*) flow parameters and (*b*) time- and space-averaged Nusselt number obtained with both types of temperature boundary condition. Filled and open symbols correspond to the cases of constant heat flux and constant cylinder temperature, respectively, and the symbols square, left triangle, delta, right triangle represent the cylinder average, front face, top face, and rear face, respectively. M and N are the number of grid points in the X and Y directions, respectively.

this quantity between the final two grid sizes is 0.15%. As it is found that the 323×264 grid size captures the structures and the details of the 2-D laminar flow very well, this grid size has been used in all further computations.

It is found that the main criteria that need to be considered for choosing the time step are the adequate resolution of the eddy-shedding frequency and the rms value of the drag and lift coefficients and local Nusselt number. The average drag and lift coefficients and average Nusselt number on the cylinder are rather insensitive to the variations in the time step. The time step was set at 10^{-3}, since a smaller time step had no significant influence on the results.

Different initial conditions corresponding to impulsive flow $(U = 1, V = 0)$, starting from rest $(U = 0, V = 0)$ and starting from rest with gradual increase in inlet velocity to unity by a sine function, were explored. All of them led to the same asymptotic dynamic flow field with negligible differences in the flow and heat transfer parameters, but the time required for the unsteady flow to become periodic varied with the initial condition. The impulsive flow initial condition has been finally used in further computations. The transition of the flow from a steady to an unsteady condition is automatically initiated by computer round-off errors, thus eliminating the need to perturb the solution.

4.3. Solution Methodology

In the present work, the finite-volume method developed by Eswaran and Prakash [26] for complex 3-D geometries on a nonstaggered grid, has been used. The semi-explicit method has been used to solve the unsteady Navier–Stokes equations in which the momentum equations are discretized in an explicit manner, with the exception of pressure gradient terms which are treated implicitly. As a consequence, the equation coupling reduces to a Poisson equation for pressure correction. Oscillations which could be generated by pressure–velocity decoupling has been avoided via the momentum interpolation proposed by Rhie and Chow [27]. In this method, two

steps are followed at every time level. First, a predicted velocity is found from the discretized momentum equation using the previous-time-level pressure field. The second, corrector, step consists of iterative solution of the pressure-correction equation and obtaining the corresponding velocity corrections such that the final velocity field satisfies continuity. The algorithm has been successfully applied on various problems [26, 28, 29].

However, the code has been substantially modified here to remove some of the features required only for nonorthogonal grids and was made strictly two-dimensional. This has been done to avoid excessive computation for the 2-D orthogonal geometry problem attempted here. Furthermore, the QUICK scheme [30] has been consistently implemented in the code while ensuring the conservative property of the finite-volume method. In the previous work by the present authors [31], implementation issues on the nonstaggered grid have been discussed with regard to the numerical accuracy and relative performance of the first-order upwind, central difference, second-order upwind, and QUICK convection schemes. It was shown that QUICK converges to a grid-independent solution with substantially fewer grid points and requires the least computational time for the same accuracy as compared to the other convection schemes.

5. RESULTS AND DISCUSSION

In the present study, the following Reynolds number flows in the 2-D regime are considered:

Steady flow: $\mathrm{Re} = 1,2$, and 5 to 40 in steps of 5.
Unsteady(periodic) flow: $\mathrm{Re} = 50$ to 160 in steps of 10.
Prandtl number has been fixed at 0.7 (as for air).

Before instantaneous and time-averaged flow and thermal fields were used for the calculation of flow and heat transfer parameters, computation was carried out for at least 20 cycles beyond the time the asymptotic shedding frequency of the Kármán vortex was attained.

5.1. Flow Pattern

Figure 4 shows the computational results in the vicinity of the cylinder by the streamlines plots at $\mathrm{Re} = 1$, 2, 40, 50, 120, and 160. The cases $\mathrm{Re} \leq 40$ are steady-state, while the cases $\mathrm{Re} \geq 50$ are unsteady periodic (where instantaneous values are shown). It can be seen in Figure 4*a* that flow is fully attached with no separation at $\mathrm{Re} = 1$. However, Figure 4*b* shows that the flow separates at the trailing edge of the cylinder at $\mathrm{Re} = 2$. As a result, a closed steady recirculating region consisting of twin symmetric vortices (a separation bubble) forms behind the cylinder. This re-circulating region increases in size with the increase in Reynolds number and the flow remains steady at $\mathrm{Re} = 40$ as shown in Figure 4*c*. However, by $\mathrm{Re} = 50$ (Figure 4*d*) , the vortices in the separation bubble start to separate alternately from the trailing edge of the square cylinder and move downstream because of Bénard-von Kármán instability (Provansal et al. [32]) in the unsteady periodic flow phenomena referred

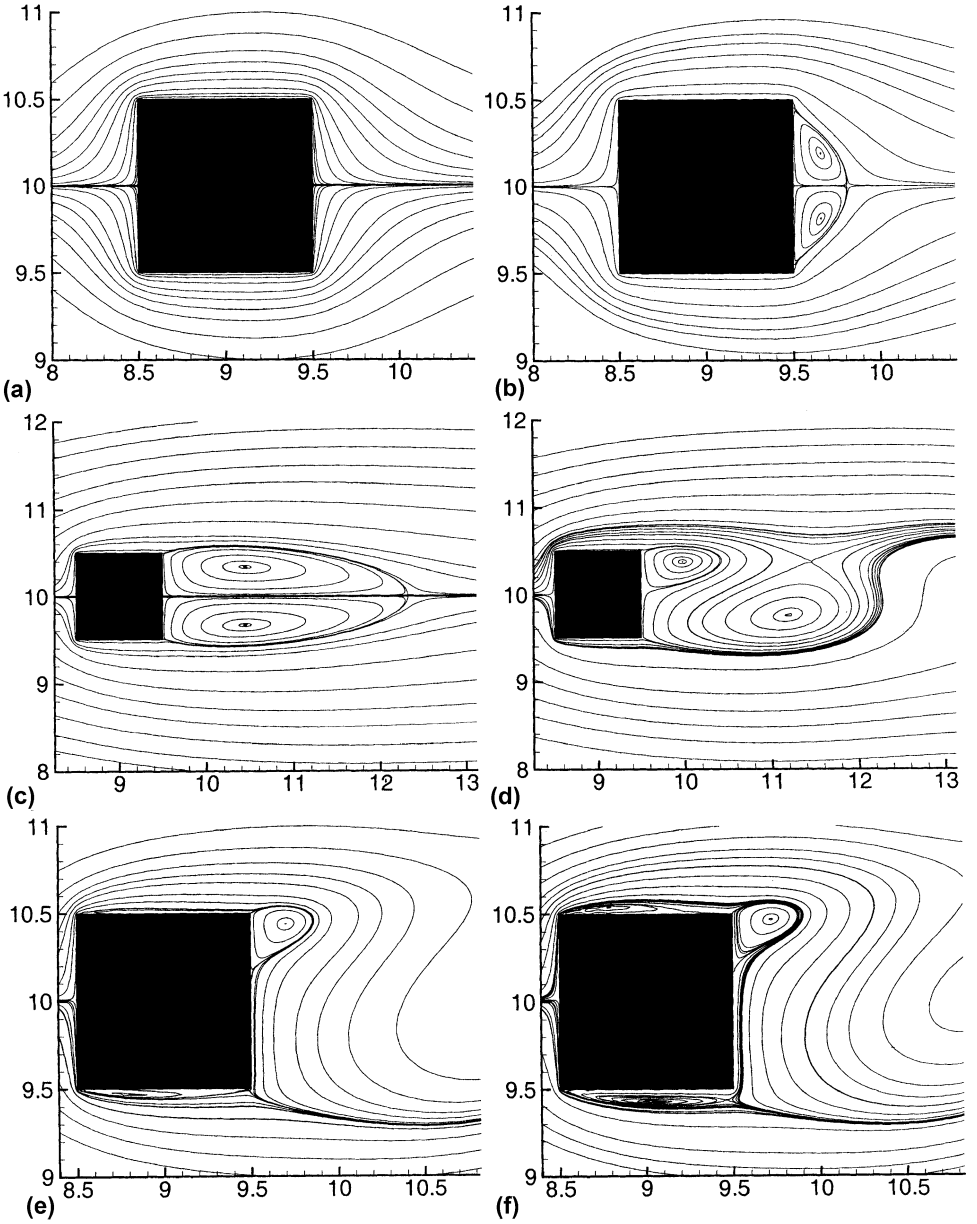

Figure 4. Streamlines (instantaneous for the periodic flow) around the square cylinder for different Reynolds numbers: (*a*) Re = 1; (*b*)Re = 2; (*c*) Re = 40; (*d*) Re = 50; (*e*) Re = 120; (*f*) Re = 160.

to as vortex shedding (while the antisymmetric wake flow pattern is normally referred to as the Kármán vortex street). At Re = 120, shown in Figure 4*e*, the flow separates at the leading edge of the cylinder and reattaches a short distance downstream, thus forming small recirculation regions on the side faces of the cylinder. In the instantaneous picture shown in Figure 4*f*, Re = 160, the separation occurs at

the leading edges with no reattachment on the bottom face of the cylinder. Indeed, there is entrainment of the fluid from the wake to the bottom region of the cylinder, as is indicated by the streamlines pattern. Thus, in the 2-D laminar regime for the square cylinder, there seem to be five distinct flow patterns: first, creeping steady laminar flow without separation; second, steady flow separation at the trailing edge with a separation bubble trapped behind the cylinder; third, unsteady flow separation at the trailing edge with vortex shedding; fourth, separation at the leading edge and reattachment on the sides of the cylinder; and fifth, separation at the leading edges with no reattachment on either the top or bottom face of the cylinder. Vortex shedding occurs in the third, fourth, and fifth cases, while the first two cases are of steady flow.

The *instantaneous* streamlines in Figures 5*a*–5*h* show the detailed views of the laminar vortex shedding near the square cylinder at $\mathrm{Re} = 100$, for eight successive moments of time which span over the whole period (i.e., Figure 5*a* is repeated after Figure 5*h* for the next cycle of vortex shedding). The critical points of the streamline patterns described by Perry et al. [33], such as centers and saddles, are also shown in the figure. As discussed by Eaton [34] for the circular cylinder, Figures 5*d*–5*g* show a vortex shedding from the top of the cylinder while fluid from below the cylinder is drawn up into the recirculation region. The vortex that is forming on the bottom of the rear face of the cylinder grows until it reaches the point where it breaks off, shown in Figure 5*h*. The shedding process is repeated in Figure 5*h*–5*c*. One of the most prominent features of the streamline pattern is what Perry called the instantaneous *alleyways*, which are the paths along which fluid is drawn from above or below the cylinder into the recirculation region. These appear in Figures 5*d*–5*g*, for example, where an instantaneous alleyway carries fluid from below the cylinder around the forming vortex and up between the shedding vortex and the cylinder to the top of the recirculation region. Similar observation was made by Zdravkovich [35] for the circular cylinder. For the circular cylinder, Eaton [34] has pointed out a qualitative discrepancy between his results and the vortex shedding model proposed by Perry et al. [33]. While Eaton's Figure 1 shows the center and saddle of a shedding vortex approaching each other and disappearing before a new vortex is shed, Perry et al.'s Figure 2 shows the centers and saddles of two shed vortices coexisting. Our results shown in Figure 5 conform to Eaton's picture of laminar vortex shedding.

Figure 6 shows the *time-averaged* streamlines in the 2-D shedding state. Figure 6*a* shows the trailing edge separation at $\mathrm{Re} = 100$. At $\mathrm{Re} = 110$ (Figure 6*b*), the flow separates from the leading edge as well and reattaches at a short distance downstream, thus forming small recirculation regions on the top and bottom faces of the cylinder. With increasing Reynolds number these recirculation regions elongate, and eventually at $\mathrm{Re} = 150$ the re-attachment point reaches very close to the trailing edge of the cylinder as shown in Figure 6*c*. At $\mathrm{Re} = 160$ (Figure 6*d*), the reattachment point moves past the trailing edge and the fluid from the wake enters the top and bottom regions of the cylinder. Thus, there are three different time-averaged flow patterns for the periodic flow: no flow separation from the sides, separation and reattachment on the sides, and finally, separation at the leading edge but no reattachment on the sides, observed at $50 \leq \mathrm{Re} \leq 100$, $110 \leq \mathrm{Re} \leq 150$, and $\mathrm{Re} = 160$, respectively, in the present work.

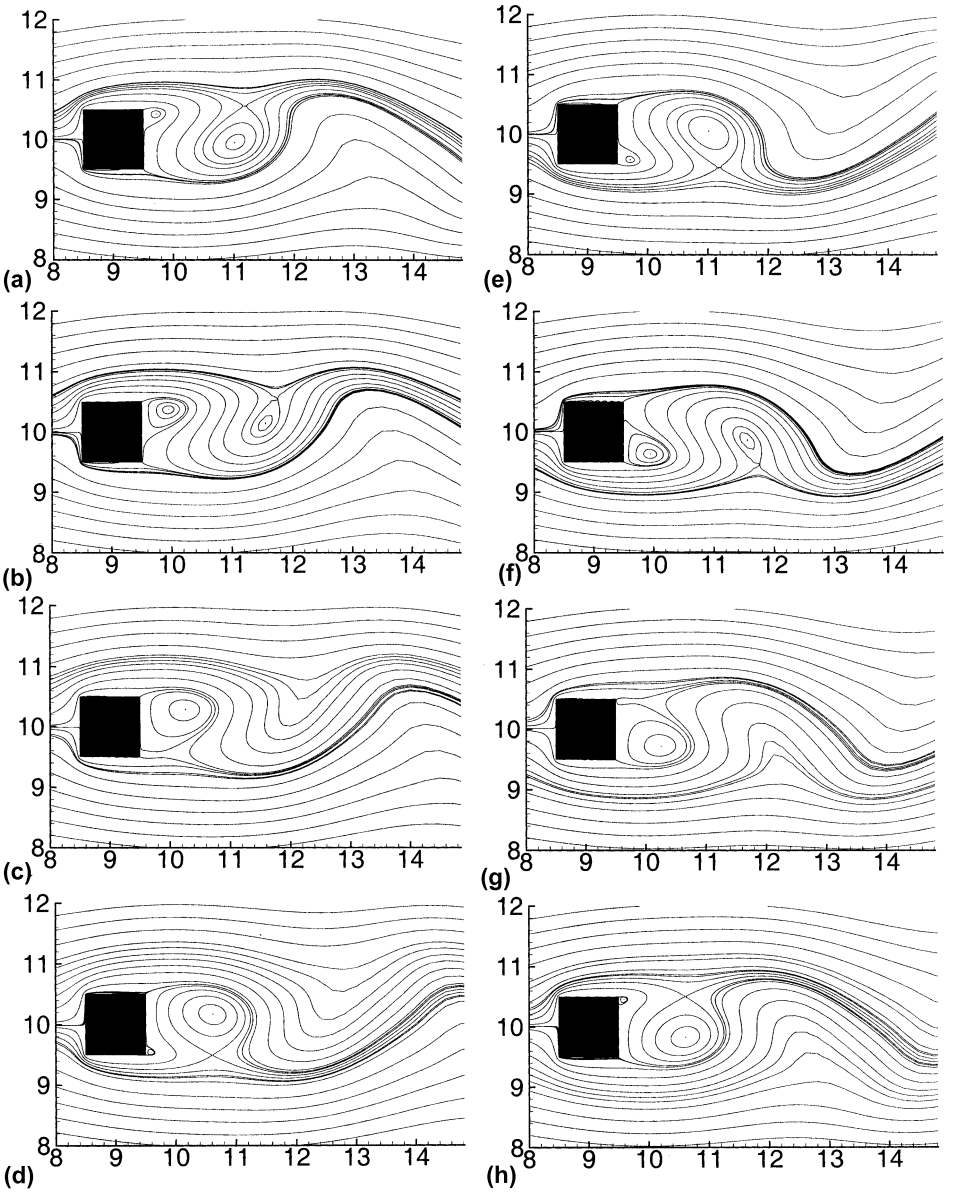

Figure 5. Instantaneous streamlines near the square cylinder, separated by an interval of one-eighth of the time period of vortex shedding, at $\mathrm{Re} = 100$.

From a numerical linear stability analysis at a blockage ratio of 14.3%, Kelkar et al. [24] reported the Reynolds number for the onset of vortex shedding for the square cylinder as 53, whereas in the practically zero-blockage experiments of Norberg and co-workers [11], its value is estimated to be in the range 47 ± 2. Sohankar et al. [13] reported its value to be 51.2 ± 1.0 at a blockage ratio of 5%. Previous numerical work by Sohankar et al. [10, 11] shows that the separation

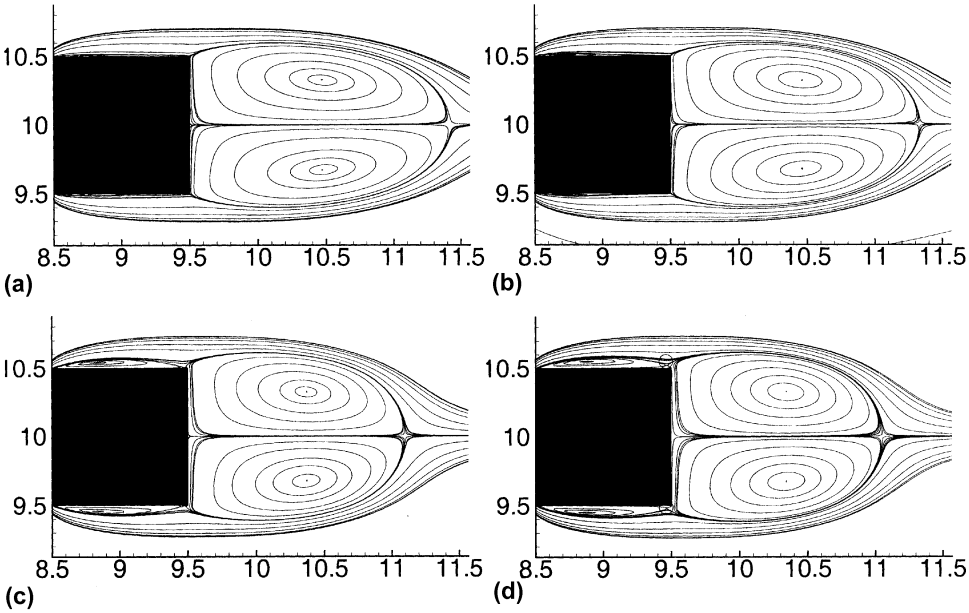

Figure 6. Time-averaged streamlines near the square cylinder at (*a*) Re = 100; (*b*) Re = 110; (*c*) Re = 150, and (*d*) Re = 160 (inviscid saddle points, near the rear end corner, are marked by a circle).

for $\mathrm{Re} \leq 100$, at all times occurs from the trailing edge, predominantly from the trailing edge at Re = 125, predominantly from the leading edge at Re = 150, and, finally, always from the leading edge for $\mathrm{Re} \geq 175$. Franke et al. [7] report separation to occur from leading edge for $\mathrm{Re} > 150$ at a blockage ratio of 8.3%. Robichaux et al. [16] report the results at a blockage ratio of 5.56% and found that the flow separation from forward edges starts at Re = 120, and eventually at Re = 150 the reattachment point moves past the trailing edge over part of the shedding cycle. Thus, the present results are in good agreement with the previous work.

5.2. Isotherms' Pattern

Figures 7*a*–7*h* show the instantaneous isotherms near the square cylinder for Re = 100 at the same instants of time for which streamlines have been shown in Figures 5*a*–5*h*. The isotherms exhibit wavering motion as well as streamwise stretching. As they continue to move downstream, the downstream tip of each of them is finally disconnected from the upstream main body. For instance, in Figures 7*d*–7*g*, the neck of the isotherm, connecting its downstream tip with its main body still closer to the cylinder, of value 0.21, is stretched and pushed downward. Thereafter, bending and thinning of the neck occur until it is disconnected, shown in Figure 7*h*. This obviously occurs when the vortex forming from the bottom of the rear surface of the cylinder also breaks off, shown in Figure 5*h*.

Figure 8 shows isotherms and those streamlines which separate the main flow and the separated-flow region, so as to discern the effect of the recirculation region on the isotherms and heat transfer from the cylinder in the separated region.

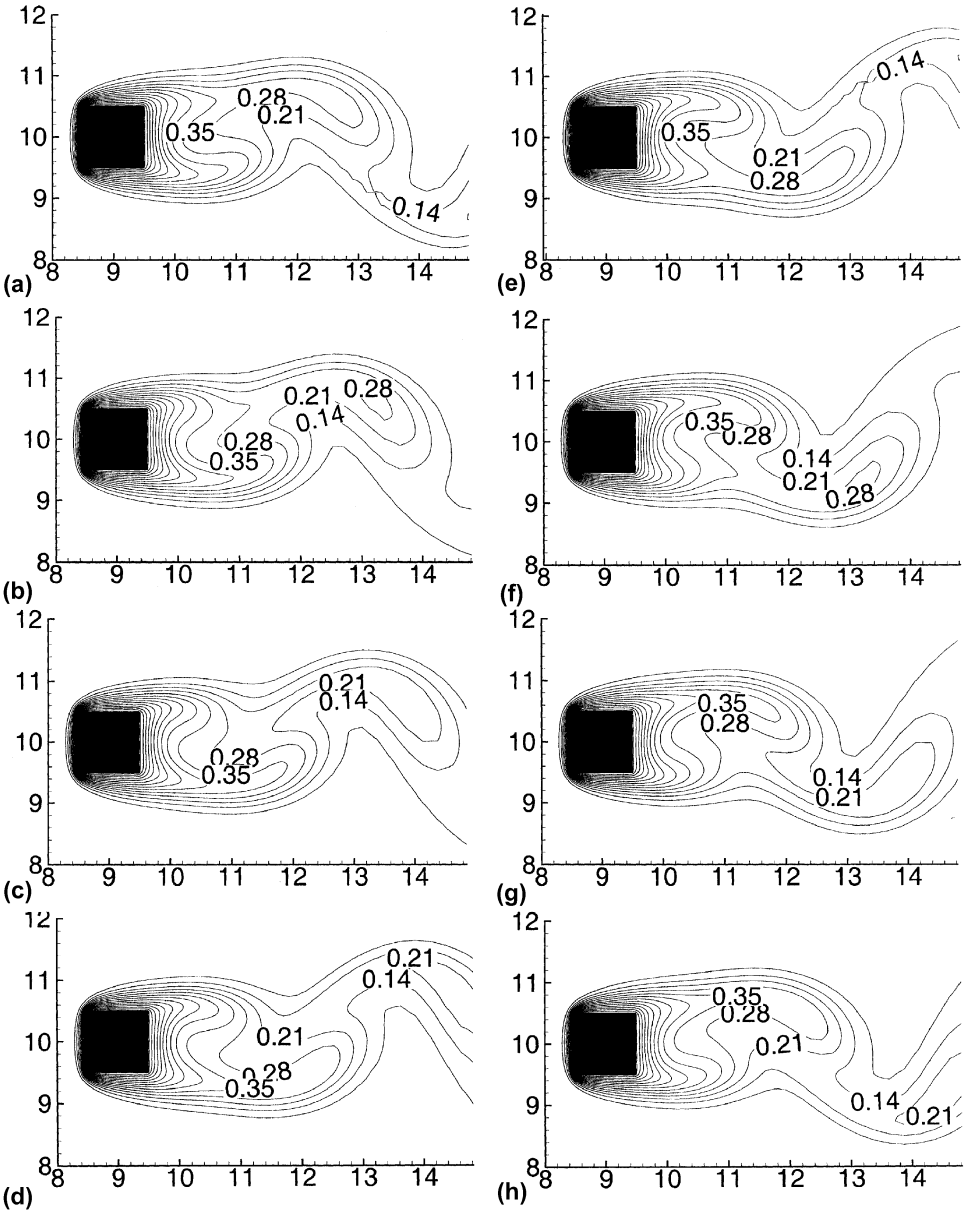

Figure 7. Instantaneous isotherms near the square cylinder, separated by an interval of one-eighth of the time period of vortex shedding, at Re = 100, for the constant cylinder temperature case.

The steady cases, Figures 8*a*–8*d*, and the time-averaged result of the unsteady periodic cases, Figures 8*e*–8*h*, are symmetric. Thus, the isotherms for the constant cylinder temperature and constant heat flux case are shown in Figure 8 above and below the horizontal axis, respectively. The figure shows that there is crowding of isotherms only over those portions where the flow has not separated. The maximum

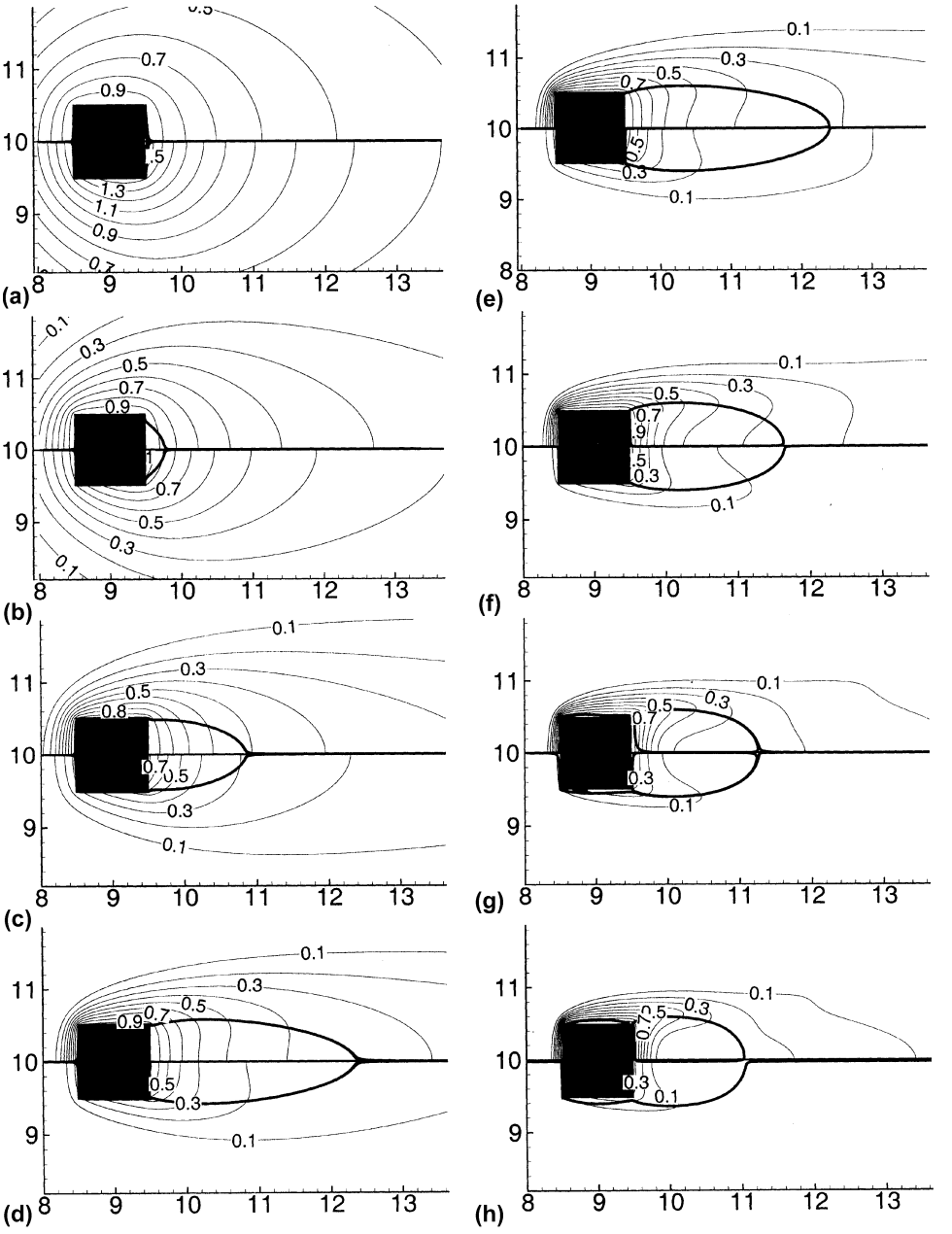

Figure 8. Streamlines separating the main flow and the separated-flow region (shown by thick lines) and isotherms (upper and lower half represent the results for the constant cylinder temperature and constant heat flux cases, respectively) for different Reynolds numbers: (*a*) Re = 1; (*b*) Re = 5; (*c*) Re = 20; (*d*) Re = 40; (*e*) Re = 50; (*f*) Re = 80; (*g*) Re = 120; (*h*) Re = 160. The periodic results for (*e*)–(*h*) correspond to the time-averaged flow and thermal fields.

crowding of the isotherms is seen on the front face, indicating the highest Nusselt number, as compared to other surfaces of the cylinder, since the thermal boundary-layer growth starts from this face. With the increase in Reynolds number, it is worth noting that the recirculation length increases for the steady flow case and decreases for the periodic flow, while the crowding of isotherms near the rear surface of the cylinder in the recirculation region increases for both types of flow. The effect of vortex shedding is clearly seen in Figures 8*e*–8*h*, with the considerable change in the shape of the isotherms in the recirculation region for the periodic flow as compared to steady-flow case. The isotherms are widely spread over a long recirculation region at $\mathrm{Re} = 50$ and are more closely packed for the shorter recirculation region at $\mathrm{Re} = 160$. Furthermore, the isotherms come closer to the rear surface of the cylinder in the recirculation region with increasing Reynolds number. This is due to the re-circulation of a larger amount of fluid in the steady flow regime and rolling of the Kármán vortices closer to the cylinder in the periodic flow regime.

5.3. Steady Flow: $1 \leq \mathrm{Re} \leq 40$

5.3.1. Recirculation Length. The recirculation length, defined as the streamwise distance from the base of the cylinder to the re-attachment point along the wake centerline, has an empirical relationship, for the circular cylinder for $4.4 \leq \mathrm{Re} \leq 40$ (Zdravkovich [1]),

$$\frac{L_r}{B} = 0.05 \times \mathrm{Re} \tag{6}$$

which is shown in Figure 9*a*. This figure also shows the computed values of the recirculation length for the square cylinder, for which a linear curve-fit by the least-

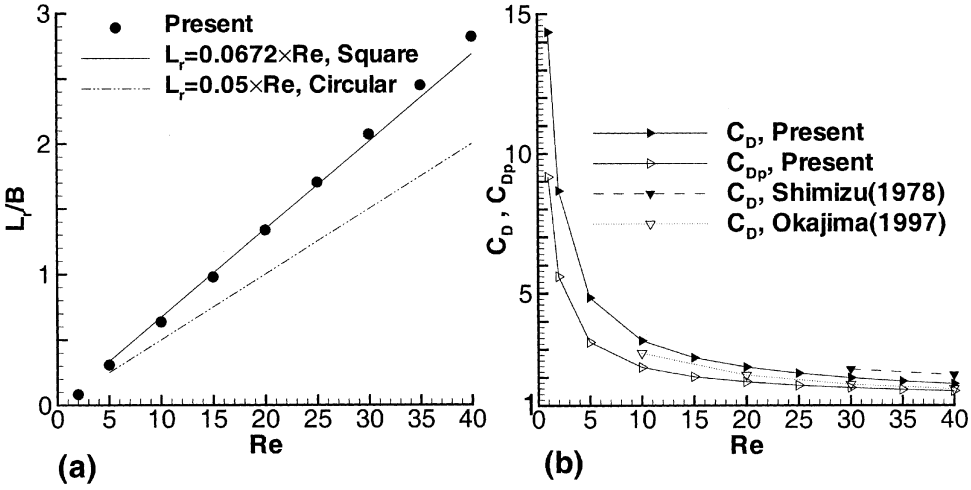

Figure 9. Variation of (*a*) recirculation length and (*b*) coefficient of total and pressure drag with Reynolds number for the steady flow.

squares method leads to the following expression (with a maximum deviation of 5%) for $5 \leq \mathrm{Re} \leq 40$:

$$\frac{L_r}{B} = 0.0672 \times \mathrm{Re} \tag{7}$$

also shown in Figure 9*a*. The figure clearly shows that the recirculation length for the unconfined square cylinder flow is larger than for its circular counterpart, and this difference increases with increasing Reynolds number.

5.3.2. Drag coefficient. Drag force is produced by viscous friction along the surface and by an unsymmetric pressure distribution on the upstream and downstream sides of the cylinder. The drag coefficient can be partitioned as $C_D = C_{Dv} + C_{Dp}$ with the viscous drag coefficient $C_{Dv} \equiv F_{Dv}/\frac{1}{2}\rho u_\infty^2 B$ and pressure drag coefficient $C_{Dp} \equiv F_{Dv}/\frac{1}{2}\rho u_\infty^2 B$, where F_{Dv} and F_{Dp} are viscous and pressure drag forces obtained by integrating the viscous shear and pressure forces over the surface of the cylinder, respectively.

The viscous drag, which determines the difference between C_D and C_{Dp}, while less than the pressure drag, is nonetheless significant in this low Reynolds number range, as is seen in Figure 9*b* which also shows that the drag coefficient varies strongly with Re in the steady-flow regime. The figure further shows that the drag coefficient obtained in the present work lies between the experimental results of Shimizu and Tanida [3] and the numerical results of Okajima et al. [12].

5.4. Unsteady Periodic Flow: $50 \leq \mathrm{Re} \leq 160$

5.4.1. Mean recirculation length. The length of the recirculation region of the time-averaged flow field is shown in Figure 10*a* for the range of periodic flow Reynolds numbers. This figure shows the monotonic decrease in the mean wake

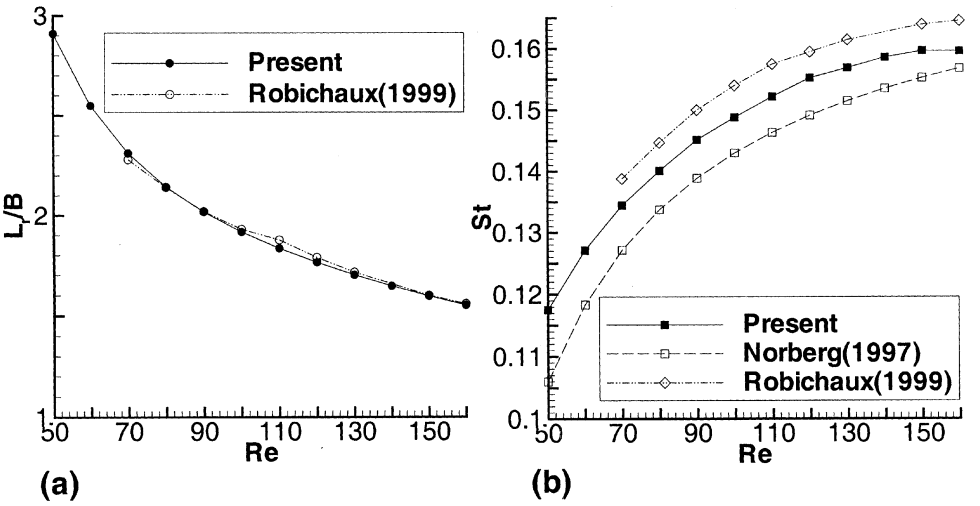

Figure 10. Variation of (*a*) mean recirculation length and (*b*) Strouhal number with Reynolds number for the periodic flow.

length with increasing Reynolds number for periodic flow, in contrast to its linear increase in the steady-flow regime. This trend is consistent with the 2-D flow over the circular cylinder. The figure further shows that the present simulations agree closely with the results of Robichaux et al. [16].

5.4.2. Strouhal number. An important quantity in unsteady periodic flow is the vortex shedding frequency, normally expressed in nondimensional terms as the Strouhal number ($\mathrm{St} = fB/u_\infty$). A fast Fourier transform of the time series for the lift coefficients is used to determine the Strouhal number. Figure 10*b* shows the Strouhal versus Reynolds number variation obtained in the present simulations along with the corresponding numerical results of Robichaux et al. [16] and the experimental work of Norberg et al. [11]. All the results show a monotonic increase in Strouhal number with the Reynolds number. The Strouhal number obtained in the present work lies between the results obtained by Norberg et al. [11] and Robichaux et al. [16], while the trend remains the same. The difference in the numerical results may be due partly to the difference in the blockage ratio used in the simulations. In the present work, $\beta = 5\%$ was used, as compared to $\beta = 5.56\%$ used by Robichux et al. [16]. The number of grid points used in the present simulations were, however, 85,272, compared to 15,000 by Robichux et al. [16].

Figure 10*b* shows that the Strouhal number increases asymptotically with increasing Reynolds number. However, there is a slight reduction in Strouhal number at $\mathrm{Re} = 160$, probably due to the widening of the wake as the mean flow fully detaches from the leading edge of the cylinder, shown in Figure 6*d*.

5.4.3. Drag and lift coefficient. In Figure 11*a*, the variation of the time-averaged value of the coefficient of total drag and pressure drag versus Reynolds number is plotted along with the results of Sohankar et al. [10]. The mean drag coefficient obtained in the present simulation is also compared with the experimental results of Shimizu and Tanida [3] and the numerical results of Franke et al. [7]

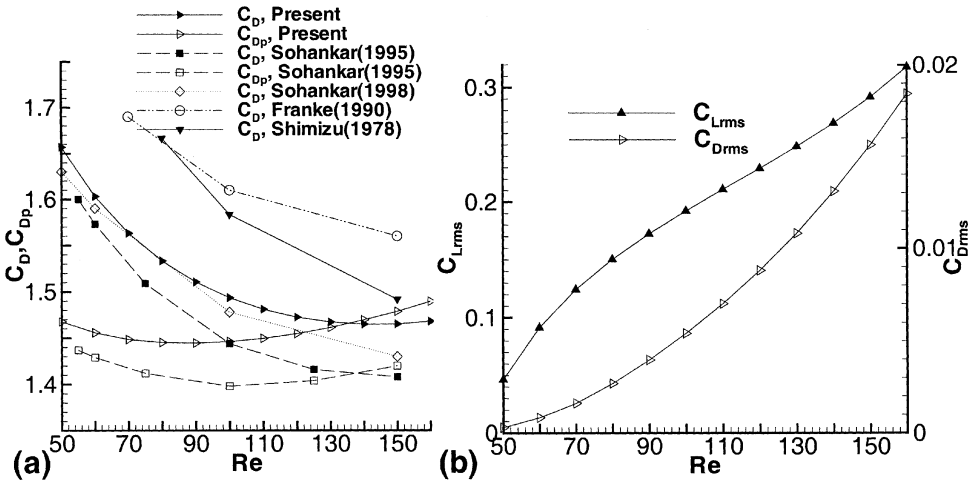

Figure 11. Variation of (*a*) time-averaged value of coefficient of total drag and pressure drag and (*b*) rms value of lift and drag coefficient with Reynolds number for the unsteady periodic flow.

and Sohankar et al. [13]. The trend of variation of both drag coefficients, obtained from the present work and Sohankar et al. [10], is similar, with a maximum deviation of 4%. It also shows that the time averaged viscous drag coefficient ($= C_D - C_{Dp}$) is positive up to Re $= 130$ in the present work, whereas the corresponding value was 125 in the simulations by Sohankar et al. [10]. The small recirculation region on the top and bottom surfaces of the cylinder leads to negative viscous drag at Re ≥ 140, in the present work. Note, however, that a finer 363×264 grid size has been used in the present work, as compared to 128×86 used by Sohankar et al. [10]. The time-averaged drag coefficient in the latter work of Sohankar et al. [13], which also uses a fine grid, agrees more closely with ours, with a maximum deviation of only 2%. The values obtained by Shimizu and Tanida [3] and Franke et al. [7] (on a grid size of 88×76 and $\beta = 8.34\%$) are somewhat higher. Nevertheless, the trend remains the same.

The rms values of drag and lift coefficients give a measure of the amplitude of the unsteady cylinder wake oscillations. The variation with Reynolds number is shown in Figure 11*b*. Although the order of magnitude of the rms drag coefficient is one order lower than that of the rms lift coefficient, both quantities increase monotonically with the Reynolds number.

5.5. Steady and Unsteady Heat Transfer: $1 \leq \mathrm{Re} \leq 160$

In most applications it is not necessary to know in detail the local temperature field, but only the overall heat transfer between the body and fluid. This quantity is expressed conveniently through the average Nusselt number. The *local* Nusselt number is defined in this study as $\mathrm{Nu}_L \equiv hB/k$ and is equal to $-\partial\theta/\partial n$ (n represent the direction normal to the surface of the cylinder) for the constant cylinder temperature, and to $1/\theta_W$ (W represents the surface of the cylinder) for the constant heat flux case. For steady flow, the average Nusselt number for each surface of the square cylinder is obtained by averaging the local Nusselt number over the surface. Finally, the cylinder Nusselt number is obtained by averaging these values. In the unsteady periodic flow, the surface-averaged values are also time-averaged over a certain integer number of cycles of vortex shedding.

For the constant cylinder temperature, the cylinder Nusselt number at Re $=$ 100 obtained in the present study is 4.04, while Kelkar et al. [24] and Rosales [36] predict a value of 3.25 and 3.9, respectively. It is worth noting that Kelkar et al. [24] and Rosales [36] have used blockage ratio of 14.3% and 7.7% and grid size of 80×80 and 172×114, respectively whereas the corresponding values in the present work are 5% and 323×264. Unfortunately, a comparison with the experimental results could not be done due to the unavailability of the forced-convection heat transfer results for this configuration at Re ≤ 160.

Figure 12 shows the variation of the average cylinder Nusselt number, as well as that of each surface separately, versus the Reynolds number for both boundary conditions used. The front surface consistently displays the highest Nusselt number, the top and bottom surface value is intermediate, followed by the rear surface. The rear Nusselt number is more strongly dependent on Reynolds number in the unsteady periodic flow as compared to the steady flow regime, as is indicated by the increased slope of the curve in the unsteady periodic regime. However, the opposite

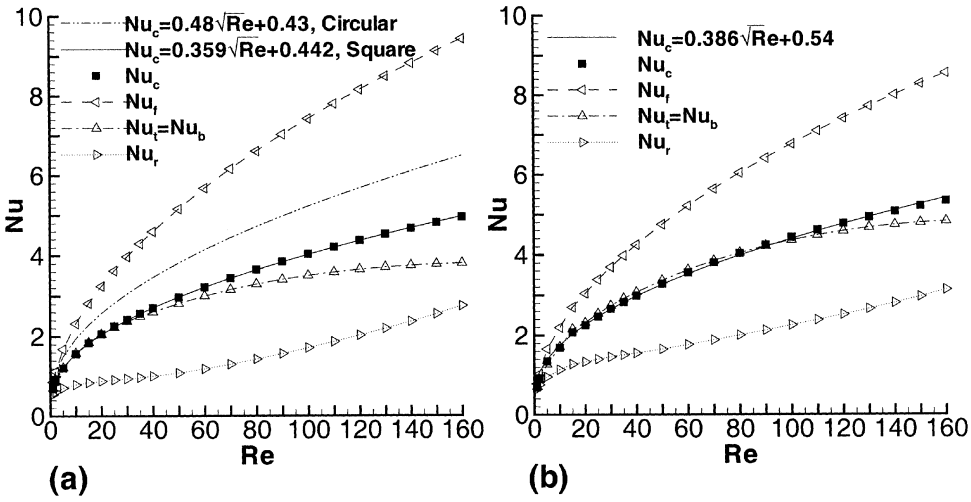

Figure 12. Nusselt number (time-averaged for the periodic flow) for the cylinder and each of its face as a function of Reynolds number for (*a*) constant cylinder temperature case and (*b*) constant heat flux case. Subscripts: f, front; t, top; r, rear; b, bottom; c, cylinder average.

trend is observed for the other surfaces. Therefore, it seems that the effect of vortex shedding on the heat transfer from the cylinder is felt mainly by the rear surface. This is because separation occurs at the trailing edge of the cylinder for the time-averaged flow field on all the Reynolds numbers in the unsteady periodic flow regime explored, except $\mathrm{Re} = 160$. The rear surface is cooled by an alternating separating and reattaching flow whose magnitude is coupled to the Reynolds number. Figure 12*a* shows that the Nusselt number for the cylinder is greater than its value on the top face in the periodic flow regime, whereas they are almost equal in the steady flow regime.

Eckert et al. [37] have given the following empirical expression for the constant-temperature circular cylinder Nusselt number, with a deviation of 4% with the experimental values in the Reynolds number range from 1 to 4,000:

$$\mathrm{Nu}_c = 0.48\sqrt{\mathrm{Re}} + 0.43 \tag{8}$$

which is plotted in Figure 12*a*. It has been pointed out by Eckert et al. [37] that the Nusselt number for any 2-D laminar boundary-layer region is proportional to the square root of the Reynolds number as long as the boundary-layer thickness may be regarded as small; the constant in Eq. (8) allows for the fact that at low Reynolds number the boundary-layer thickness becomes considerable as compared to the cylinder diameter. We propose the correlation for the square cylinder:

$$\mathrm{Nu}_c = 0.359\sqrt{\mathrm{Re}} + 0.442 \tag{9}$$

for $5 \leq \mathrm{Re} \leq 160$, which is plotted in Figure 12*a*. This has a maximum deviation of 1% for $10 \leq \mathrm{Re} \leq 160$ and less than 3% at $\mathrm{Re} = 5$ with the computed results.

It shows that the average Nusselt numbers for the square cylinder are less than for the circular one.

A similar correlation for the constant heat flux case with a maximum deviation of 4% is plotted in Figure 12*b* and is given by

$$\mathrm{Nu}_c = 0.386\sqrt{\mathrm{Re}} + 0.54 \tag{10}$$

for $5 \leq \mathrm{Re} \leq 160$.

6. CONCLUSIONS

This study focuses on the unconfined flow and heat transfer characteristic around a square cylinder in the 2-D laminar regime ($1 \leq \mathrm{Re} \leq 160$). The flow for $\mathrm{Re} \leq 40$ is steady, while that for $\mathrm{Re} \geq 50$ is unsteady periodic, with the transition to unsteadiness occurring between $\mathrm{Re} = 40$ and $\mathrm{Re} = 50$. In terms of separation, three different onset values have been predicted: the first is the onset of separation between $\mathrm{Re} = 1$ and $\mathrm{Re} = 2$; the second, onset of vortex shedding (with trailing-edge separation) between $\mathrm{Re} = 40$ and $\mathrm{Re} = 50$; and the third, onset of leading-edge separation between $\mathrm{Re} = 100$ and $\mathrm{Re} = 110$. The model of laminar vortex shedding shown by our computed streamlines pattern for the square cylinder matches with that for the circular cylinder as described by Eaton [34]. A correlation between the nondimensional recirculation length and Reynolds number has been proposed for $5 \leq \mathrm{Re} \leq 40$ in the steady flow regime. For periodic flow, our results show excellent agreement with the available numerical and experimental data. With increasing Reynolds number, the recirculation length increases for steady flow, whereas for the mean periodic flow it decreases monotonically. The time-averaged viscous drag coefficient is predicted to become negative between $\mathrm{Re} = 130$ and $\mathrm{Re} = 140$.

The primary focus of this study, however, has been the heat transfer from the square cylinder, which has not been extensively studied previously. Both constant-temperature and constant-heat-flux boundary conditions have been addressed, for a Prandtl number of 0.7. The heat transfer characteristics in the steady flow ($\mathrm{Re} \leq 40$) regime differ considerably from those in the unsteady periodic 2-D flow regime ($50 \leq \mathrm{Re} \leq 160$). The shedding of Kármán vortices causes a wavering motion of the instantaneous isotherms in the wake region as well as their stretching and thinning, ending with their tips being finally disconnected from the main body periodically. This causes considerable change in the shape of even time-averaged isotherms in the recirculation region as compared to the steady-flow case, and the mechanism of heat transfer especially from the rear surface of the cylinder differs significantly in the two types of flow. The cylinder average Nusselt number increases monotonically with increasing Reynolds number. For both the constant cylinder temperature and constant heat flux boundary conditions, the Nusselt number from the front surface of the cylinder is highest, the top and bottom surface values being intermediate, followed by the rear surface. The time-averaged rear-surface Nusselt number is more strongly dependent on Reynolds number in the periodic flow regime, in contrast to the other faces of the cylinder. Finally, heat transfer correlations applicable in 2-D flow regime have been proposed for both the temperature boundary conditions considered. These correlations are significantly different from those applicable to the corresponding circular cylinder problem.

REFERENCES

1. M. M. Zdravkovich, *Flow around Circular Cylinders*, Oxford University Press, New York, 1997.
2. C. H. K. Williamson, Vortex Dynamics in the Cylinder Wake, *Annu. Rev. Fluid Mech.*, vol. 28, pp. 477–539, 1996.
3. Y. Shimizu and Y. Tanida, Fluid Forces Acting on Cylinders of Rectangular Cross-Section, *Trans. Jpn. Soc. Mech. Eng. B*, vol. 44, pp. 2699–2706, 1978.
4. R. W. Davis and E. F. Moore, A Numerical Study of Vortex Shedding from Rectangles, *J. Fluid Mech.*, vol. 116, pp. 475–506, 1982.
5. A. Okajima, Strouhal Numbers of Rectangular Cylinders, *J. Fluid Mech.*, vol. 123, pp. 379–398, 1982.
6. A. Okajima, Numerical Simulation of Flow around Rectangular Cylinders, *J. Wind Eng. Ind. Aerodyn.*, vol. 33, pp. 171–180, 1990.
7. R. Franke, W. Rodi, and B. Schönung, Numerical Calculation of Laminar Vortex-Shedding Flow past Cylinders, *J. Wind Eng. Ind. Aerodyn.*, vol. 35, pp. 237–257, 1990.
8. T. Tamura and K. Kuwahara, Numerical Study of Aerodynamic Behaviour of a Square Cylinder, *J. Wind Eng. Ind. Aerodyn.*, vol. 33, pp. 161–170, 1990.
9. T. G. Zaki, M. Sen, and M. Gad-el-Hak, Numerical and Experimental Investigation of Flow past a Freely Rotatable Square Cylinder, *J. Fluids Struct.*, vol. 8, pp. 555–582, 1994.
10. A. Sohankar, L. Davidson, and C. Norberg, Numerical Simulation of Unsteady Flow around a Square Two-Dimensional Cylinder, *Proc. 12th Australian Fluid Mechanics Conf.*, Sydney, Australia, pp. 517–520, 1995.
11. A. Sohankar, C. Norberg, and L. Davidson, Numerical Simulation of Unsteady Low-Reynolds Number Flow around Rectangular Cylinders at Incidence, *J. Wind Eng. Ind. Aerodyn.*, vol. 69, pp. 189–201, 1997.
12. A. Okajima, D. Yi, A. Sakuda, and T. Nakano, Numerical Study of Blockage Effects on Aerodynamic Characteristics of an Oscillating Rectangular Cylinder, *J. Wind Eng. Ind. Aerodyn.*, vol. 67–68, pp. 91–102, 1997.
13. A. Sohankar, C. Norberg, and L. Davidson, Low-Reynolds Number Flow around a Square Cylinder at Incidence: Study of Blockage, Onset of Vortex Shedding and Outlet Boundary Condition, *Int. J. Numer. Meth. Fluids*, vol. 26, pp. 39–56, 1998.
14. D. A. Caughey, Implicit Multigrid Computation of Unsteady Flows past Cylinders of Square Cross-Section, *Comput. Fluids*, vol. 30, pp. 939–960, 2001.
15. A. Sohankar, C. Norberg, and L. Davidson, Simulation of Three-Dimensional Flow around a Square Cylinder at Moderate Reynolds numbers, *Phys. Fluids*, vol. 11, pp. 288–306, 1999.
16. J. Robichaux, S. Balachandar, and S. P. Vanka, Two-Dimensional Floquet Instability of the Wake of Square Cylinder, *Phys. Fluids*, vol. 11, pp. 560–578, 1999.
17. A. K. Saha, G. Biswas, and K. Muralidhar, Three-Dimensional Study of Flow past a Square Cylinder at Low Reynolds numbers, *Int. J. Heat Fluid Flow*, vol. 24, pp. 54–66, 2003.
18. V. T. Morgan, The Overall Convective Heat Transfer from Smooth Circular Cylinders, *Adv. Heat Transfer*, vol. 11, pp. 199–264, 1975.
19. S. C. R. Dennis, J. D. Hudson, and N. Smith, Steady Laminar Forced Convection from a Circular Cylinder at Low Reynolds Numbers, *Phys. Fluids*, vol. 11, pp. 933–940, 1968.
20. G. E. Karniadakis, Numerical Simulation of Forced Convection Heat Transfer from a Cylinder in Crossflow, *Int. J. Heat Mass Transfer*, vol. 31, pp. 107–118, 1988.
21. Y. T. Yang, C. K. Chen, and S. R. Wu, Transient Laminar Forced Convection from a Circular Cylinder Using a Body-Fitted Coordinate System, *J. Thermophys.*, vol. 6, pp. 184–188, 1992.

22. C. F. Lange, F. Durst, and M. Breuer, Momentum and Heat Transfer from Cylinders in Laminar Crossflow at $10^{-4} \leq \mathrm{Re} \leq 200$, *Int. J. Heat Mass Transfer*, vol. 41, pp. 3409–3430, 1998.
23. T. Igarashi, Fluid Flow and Heat Transfer around Rectangular Cylinders (the Case of a Width/Height Ratio of a Section of $0.33 \sim 1.5$), *Int. J. Heat Mass Transfer*, vol. 30, pp 893–901, 1987.
24. K. M. Kelkar and S. V. Patankar, Numerical Prediction of Vortex Shedding behind a Square Cylinder, *Int. J. Numer. Meth. Fluids*, vol. 14, pp. 327–341, 1992.
25. J. F. Thompson, Z. U. A. Warsi, and C. W. Mastin, *Numerical Grid Generation: Foundations and Applications*, pp. 305–310, Elsevier Science, New York, 1985.
26. V. Eswaran and S. Prakash, A Finite Volume Method for Navier–Stokes Equations, *Proc. Third Asian CFD Conf.*, Bangalore, India, vol. 1, pp. 127–136, 1998.
27. C. M. Rhie and W. L. Chow, A Numerical Study of the Turbulent Flow Past an Isolated Aerofoil with Trailing Edge Separation, *AIAA J.*, vol. 21, pp. 1525–1532, 1983.
28. V. Prabhakar, G. Biswas, and V. Eswaran, Numerical Prediction of Heat Transfer with a Built-in Oval Tube and Two Different Shaped Vortex Generators, *Numer. Heat Transfer A*, vol. 41, pp. 307–329, 2002.
29. S. Tiwari, D. Maurya, G. Biswas and V. Eswaran, Heat Transfer Enhancement in Cross Flow Heat Exchangers using Oval Tubes and Multiple Delta Winglets, *Int. J. Heat Mass Transfer*, vol. 46, pp. 2841–2856, 2003.
30. B. P. Leonard, A Stable and Accurate Convective Modelling Procedure Based on Quadratic Upstream Interpolation, *Comput. Meth. Appl. Mech. Eng.*, vol. 19, pp. 59–98, 1979.
31. A. Sharma and V. Eswaran, Conservative and Consistent Implementation and Systematic Comparison of SOU and QUICK Scheme for Recirculating Flow Computation on a Non-staggered Grid, *Proc. 2nd Int. and 29th Natl. FMFP Conf.*, Roorkee, India, pp. 351–358, 2002.
32. M. Provansal, C. Mathis, and L. Boyer, Bénard-von Kármán Instability: Transient and Forced Regimes, *J. Fluid Mech.*, vol. 182, pp. 1–22, 1987.
33. A. E. Perry, M. S. Chong, and T. T. Lim, The Vortex Shedding process behind Two-Dimensional Bluff Bodies, *J. Fluid Mech.*, vol. 116, pp. 77–90, 1982.
34. B. E. Eaton, Analysis of Laminar Vortex Shedding behind a Circular Cylinder by Computer-Aided Flow Visualisation, *J. Fluid Mech.*, vol. 180, pp. 117–145, 1987.
35. M. M. Zdravkovich, Smoke Observation of the Formation of a Kármán Vortex Street, *J. Fluid Mech.*, vol. 37, pp. 491–496, 1969.
36. J. L. Rosales, A Numerical Investigation of the Convective Heat Transfer in Confined Channel Flow past Cylinders of Square Cross-Section, Ph.D. thesis, The University of Arizona, Tucson, Az, 1999.
37. E. R. G. Eckert and E. Soehngen, Distribution of Heat Transfer Coefficient around Circular Cylinders in Cross Flow at Reynolds Numbers from 20 to 500, *J. Heat Transfer*, vol. 74, pp. 343–347, 1952.